Chapter 3

Joint least-squares migration/inversion: theory

This chapter presents inversion methods that overcome some short-comings of conventional time-lapse imaging methods. In the previous chapter, I discussed how two common post-imaging time-lapse cross-equalization methods—warping and matched filtering—can improve the quality of time-lapse images. Today, these methods, together with a wide range of specialized pre-stack and post-stack processing steps form the state-of-the-art in time-lapse seismic imaging. Although these methods are well developed, and are adequate in many field and geological scenarios, they are inadequate in many others.

Two practical scenarios where conventional time-lapse imaging methods become inadequate are in reservoirs under complex overburden and where large geometry differences exist between surveys. For example, because complex overburden causes complicated and irregular subsurface illumination, conventional data regularization methods are inadequate. Conventional methods are also typically inadequate to reconcile large differences in acquisition geometries between surveys. Such geometry differences can be caused by changes in acquisition systems, new production facilities, or natural environmental changes. In many cases, artifacts in time-lapse seismic

images that are caused by complex overburden or geometry differences may strongly contaminate production-related image differences. Unless non-production-related artifacts in time-lapse seismic images are attenuated, it is impossible to accurately relate image differences to changes in reservoir properties. Because conventional methods are inadequate in these scenarios, new time-lapse imaging methods are required.

In this chapter, I discuss extension of linear least-squares imaging methods to joint inversion of time-lapse seismic data sets. Because inversion accounts for illumination mismatches—caused by differences in acquisition geometries—and for band-limited wave-propagation effects through reservoir overburden, it provides better estimates of production-related changes in reservoir acoustic properties than conventional time-lapse imaging methods. By joint inversion, I mean that data sets from multiple surveys are inverted together by minimizing a single (joint) objective function. One important advantage of time-lapse imaging by joint (versus separate) inversion is that it enables incorporation of a priori information in the form of temporal as well as spatial constraints. Because seismic inversion is inherently ill-posed, these constraints are required to ensure that the inversion is stable and that results are geologically plausible.

Regularized joint inversion of time-lapse data sets can be solved in either the data and image domains. In this chapter, I show how these spatio-temporal constraints can be incorporated into a regularized joint least-squares inversion framework in the data and image domains. One advantage of image-domain joint inversion is that it enables the problem to be solved in a target-oriented way. Because of the target-oriented nature of time-lapse imaging, in many practical applications, image-domain inversion is preferable. Furthermore, because joint image-domain inversion is relatively computationally inexpensive, it can be repeated several times with different temporal and spatial constraints. In chapters 4, 5 and 6, I show different applications of these methods to synthetic and field data examples.

First, I review data-domain and image-domain least-squares inversion methods. Next, I develop the theory of joint least-squares inversion of time-lapse data sets. Finally, I discuss the spatial and temporal constraints used in the inversion.

SEISMIC IMAGING BY LEAST-SQUARES INVERSION

Linear least-squares inversion has been shown to improve structural and amplitude information in seismic images. For example, Nemeth et al. (1999) show that it improves imaging of incomplete seismic and ground penetrating radar data; Kühl and Sacchi (2003) show that it improves amplitude variation with angle (AVA) information in pre-stack gathers; and, Clapp (2005), Valenciano (2008), and Tang (2011) show that it improves images of reservoirs located under complex overburden. In these examples, the authors show that imaging by least-squares inversion provides more reliable results than conventional imaging by migration. In general, least-squares imaging of seismic data sets can be implemented in either the data domain or in the image domain.

Data-domain least-squares inversion: In this dissertation, I refer to methods that directly minimize the misfit between the recorded and modeled data as data-domain methods. One drawback of data-domain inversion methods is that they require migration and modeling (demigration) at every iteration (Nemeth et al., 1999; Kühl and Sacchi, 2003; Clapp, 2005). Because several iterations are required to reach convergence, in many practical applications, data-domain methods are too expensive. However, as I discuss later in chapter 4, by using phase-encoding methods, data-domain inversion of seismic data becomes practical. Such encoding can be either field-based (e.g., data acquisition with arbitrary number of simultaneous-sources (van Mastrigt et al., 2002; Hampson et al., 2008; Beasley, 2008; Berkhout et al., 2008; Howe et al., 2009)) or computer-based (i.e., phase-encoded imaging of conventional data sets (Krebs et al., 2009; Tang and Biondi, 2009; Verschuur and Berkhout, 2009; Schuster et al., 2011)). In chapter 4, I show an application of data-domain inversion to field-encoded time-lapse seismic data sets, with non-repeated geometries and relative shot times.

Image-domain least-squares inversion: Instead of the data-domain approach, the Hessian of the least-squares objective function can be approximated and the

problem solved in the image domain (Lambaré et al., 2003; Valenciano, 2008; Tang, 2011). In this approach, the input is the recorded data transformed (via migration) to the image domain—hence, both the input (migrated) and output (inverted) images have similar dimensions. Image-domain inversion has several desirable properties. First, as noted earlier, because the proposed formulations utilize pre-computed approximate (target-oriented) Hessian operators, no new migration and modeling are required during the inversion. Although, for many practical applications, the computational cost of the approximate Hessian is not trivial (Valenciano, 2008; Tang, 2011), once the Hessian is obtained, image-domain inversion can be done several orders of magnitude more cheaply than data-domain inversion. In addition, because the inversion problem is solved in the image domain, the computational domain can be reduced to only a target region around the reservoir, thereby reducing computational cost. This is particularly useful for time-lapse imaging, because the reservoir location and extent are usually well defined before seismic monitoring is performed. Furthermore, the imaging interest is usually limited to the regions within and around the reservoir. Finally, because it is computationally efficient, the image-domain inversion can be repeated quickly with different a priori constraints.

One way of obtaining inverted time-lapse images is by applying the least-squares inversion methods described above to individual data sets and then computing differences between inverted images. In this dissertation, this approach, which requires that the objective function for each survey be independently minimized, is called separate inversion. Because separate inversion allows only spatial constraints in the time-lapse inversion, it provides only limited improvements to the quality of time-lapse images. Nonetheless, because each problem is solved independently, artifacts in any one survey do not affect the results in other surveys.

Instead of inverting the data sets separately, by defining a single objective function for all data sets, time-lapse imaging can be posed as a joint inversion problem. For this joint inversion problem, data-domain operators are combinations of the modeling/migration operators of different surveys, whereas image-domain operators

are combinations of target-oriented approximations to the Hessians of different surveys. Importantly, joint inversion enables the incorporation of prior knowledge of the subsurface earth structure (e.g., reservoir location, extent and geometry), temporal constraints, and information from other sources (e.g., geological and petrophysical models) into the time-lapse imaging problem. Introduction of spatial and temporal constraints improve the quality and reliability of inverted time-lapse images.

Previous authors have discussed joint inversion applications to seismic data, such as impedance inversion (Sarkar et al., 2003) and crosswell ray-tomography (Ajo-Franklin et al., 2005). Other relevant time-lapse inversion methods include differential wave-equation velocity analysis (Albertin et al., 2006), sequential inversion with model-based regularization (Oldenborger et al., 2007; Miller et al., 2008; Routh and Anno, 2008), and differential travel-time tomography (Ajo-Franklin et al., 2007). Joint-inversion strategies are also common in medical imaging problems, including dynamic electrical impedance tomography (Schmitt and Louis, 2002; Schmitt et al., 2002) and electrocardiographic imaging (Messnarz et al., 2004; Guofa et al., 2006). Although my inversion goals differ from many of those listed, many of these formulations are directly extendable to inversion for time-lapse reflectivity amplitudes.

I consider two related formulations for regularized joint least-squares inversion of time-lapse seismic data sets. In the first formulation, called regularized joint inversion of multiple images (RJMI), I invert for seismic images for each input survey. In the second formulation, called regularized joint inversion for image differences (RJID), I invert for a static baseline image and for image differences between surveys. Both formulations allow for spatial and temporal constraints in the inversion. Without temporal constraints, both formulations yield results that are comparable to those from spatially regularized separate inversion. Both the RJID and RJMI formulations can be implemented in either the data domain or in the image domain.

In all the examples discussed in this dissertation, where applicable, the spatial regularization operator is a system of non-stationary dip-filters, whereas the temporal regularization operator is a gradient between surveys. First, I compute dips from the baseline image using the plane-wave destruction method (Fomel, 2002). I then

compute non-stationary dip-filters based on factorized directional Laplacians (Hale, 2007). In a later section, I discuss the spatial and temporal regularization operators in more detail.

In the next section, I discuss linear least-squares inversion of time-lapse data sets in the data and image domains.

THEORY OF SEISMIC IMAGING BY LEAST-SQUARES INVERSION

From the Born approximation of the linearized acoustic wave equation, for a known velocity model, the synthetic seismic data d^s recorded by a receiver at $\mathbf{x}_r$ due to a shot at $\mathbf{x}_s$ is given by

$$d^s(\mathbf{x}_s, \mathbf{x}_r, \omega) = \omega^2 \sum_{\mathbf{x}} f_s(\omega) G(\mathbf{x}_s, \mathbf{x}, \omega) G(\mathbf{x}, \mathbf{x}_r, \omega) m(\mathbf{x}), \tag{3.1}$$

where ω is frequency, $m(\mathbf{x})$ is *reflectivity* at image points $\mathbf{x}$, $f_s(\omega)$ is the source waveform, and $G(\mathbf{x}_s, \mathbf{x}, \omega)$ and $G(\mathbf{x}, \mathbf{x}_r, \omega)$ are Green's functions from $\mathbf{x}_s$ to $\mathbf{x}$ and from $\mathbf{x}$ to $\mathbf{x}_r$, respectively.

Taking the true recorded data at $\mathbf{x}_r$ to be d^{obs}, I define a quadratic cost function given by

$$S(\mathbf{m}) = \|d^s(\mathbf{x}_s, \mathbf{x}_r, \omega) - d^{obs}(\mathbf{x}_s, \mathbf{x}_r, \omega)\|_2. \tag{3.2}$$

As shown by previous authors (Plessix and Mulder, 2004; Valenciano, 2008), the gradient $g(x)$ of this cost function (summed over all frequencies, sources and receivers) with respect to the reflectivity is given by the real part of

$$g(\mathbf{x}) = \sum_w \omega^2 \sum_{\mathbf{x}_s} \sum_{\mathbf{x}_r} f_s(\omega) G(\mathbf{x}_s, \mathbf{x}, \omega) G(\mathbf{x}, \mathbf{x}_r, \omega) \left(\bar{d}^s(\mathbf{x}_s, \mathbf{x}_r, \omega) - \bar{d}^{obs}(\mathbf{x}_s, \mathbf{x}_r, \omega) \right), \tag{3.3}$$

and the Hessian (matrix of second derivatives) is the real part of

$$H\left(\mathbf{x},\mathbf{x}'\right)=\sum_{w}\omega^{4}\sum_{\mathbf{x}_s}\left|f\left(s\right)\right|^{2}G(\mathbf{x}_s,\mathbf{x},\omega)\bar{G}(\mathbf{x}_s,\mathbf{x}',\omega)\sum_{\mathbf{x}_r}G(\mathbf{x},\mathbf{x}_r,\omega)\bar{G}(\mathbf{x}',\mathbf{x}_r,\omega), \quad (3.4)$$

where $\mathbf{x}'$ denotes all image points and $\bar{G}$ is the complex conjugate of G. Plessix and Mulder (2004) and Valenciano (2008) discuss this derivation in detail.

Using matrix and vector notations, equation 3.1 can be written as

$$\mathbf{d}=\mathbf{L}\mathbf{m}, \quad (3.5)$$

and the objective function in equation 3.2 becomes

$$S(\hat{\mathbf{m}})=\|\mathbf{d}-\mathbf{d}^{obs}\|_2=\|\mathbf{L}\mathbf{m}-\mathbf{d}^{obs}\|_2 \quad (3.6)$$

where $\mathbf{L}$ denotes the linear Born modeling operator, $\mathbf{m}$ denotes the reflectivity model, and vectors $\mathbf{d}$ and $\mathbf{d}^{obs}$ denote the modeled and recorded data from all sources, respectively. The least-squares inverted model $\hat{\mathbf{m}}$ satisfies the equation

$$\hat{\mathbf{m}}=(\mathbf{L}^{T}\mathbf{L})^{\dagger}\mathbf{L}^{T}\mathbf{d}=\mathbf{H}^{\dagger}\tilde{\mathbf{m}}, \quad (3.7)$$

where $\mathbf{H}=\mathbf{L}^{T}\mathbf{L}$ is the Hessian of the cost function (equation 3.6), $\tilde{\mathbf{m}}$ is the migrated image, and superscripts T and $\dagger$ denote conjugate transpose and pseudo-inverse, respectively.

As discussed in the previous section, there are two ways of obtaining the inverted image $\hat{\mathbf{m}}$:

1. Minimizing the cost function in equation 3.6 such that the modeled and recorded data are similar:

$$S(\hat{\mathbf{m}})=\|\mathbf{L}\mathbf{m}-\mathbf{d}^{obs}\|_2\approx 0. \quad (3.8)$$

   This represents the data-domain approach to least-squares inversion.

2. Computing an approximation of the Hessian and then minimizing the difference

between the migrated image and the Hessian times the inverted reflectivity:

$$\mathbf{H}\hat{\mathbf{m}} \approx \tilde{\mathbf{m}}. \tag{3.9}$$

This represents the image-domain approach to least-squares inversion.

Data-domain versus image-domain inversion

Although results of data-domain and image -domain inversion are theoretically equivalent, the optimal implementation domain depends on the imaging goals, the acquisition geometry and the problem size. Below, I compare the two:

1. Data-domain inversion does not require pre-computation of an approximate Hessian matrix, whereas image-domain inversion does. However, as discussed below, there are practical methods of reducing the computational cost of the Hessian.

2. In data-domain inversion, each iteration requires at least one migration and one modeling, whereas in image-domain inversion, each iteration requires relatively cheap matrix-vector multiplication.

3. In general, data-domain inversion is slow for conventional acquisition geometries, whereas, once the approximate Hessian is computed, image-domain inversion is fast.

4. It is difficult to pose data-domain inversion as a target-oriented problem, whereas image-domain inversion is easily solved as a target-oriented problem.

5. Data-domain inversion of encoded/simultaneous-source data is relatively cheap, whereas image-domain inversion of such data is expensive in both computation and storage requirements because the Hessian is far from being diagonally dominant.

Approximating the Hessian

For any practical application, because of the large computational cost, it is infeasible (and unnecessary) to compute the full Hessian matrix defined in equation 3.4. Previous authors have discussed approximations that reduce the computational cost or that remove the need for explicit estimation of the full Hessian (Santosa and Symes, 1988; Rickett, 2003; Guitton, 2004; Plessix and Mulder, 2004; Yu et al., 2006; Symes, 2008; Valenciano, 2008; Tang, 2011).

In this dissertation, I follow the target-oriented approximation of Valenciano (2008) and Tang (2011). Because for conventional geometries, the Hessian is diagonally-dominant, it can be approximated by computing limited number of off-diagonal elements. Furthermore, because reservoirs are limited in extent, the region of interest is usually smaller than the full image space; therefore, the Hessian can be explicitly computed for that region. The Hessian for each image point within this target region $\mathbf{x}_T$ is then given by (Valenciano, 2008)

$$H\left(\mathbf{x}_T, \mathbf{x}_{T+a_x}\right)) = \sum_w \omega^4 \sum_{\mathbf{x}_s} |f(s)|^2 G(\mathbf{x}_s, \mathbf{x}_T, \omega) \bar{G}(\mathbf{x}_s, \mathbf{x}_{T+a_x}, \omega) \sum_{\mathbf{x}_r} G(\mathbf{x}_T, \mathbf{x}_r, \omega) \bar{G}(\mathbf{x}_{T+a_x}, \mathbf{x}_r, \omega), \tag{3.10}$$

where $\mathbf{x}_{T+a_x}$ represent neighboring image points. For any image point, $\mathbf{H}\left(\mathbf{x}_T, \mathbf{x}_{T+a_x}\right)$ represents a row of a sparse Hessian matrix $\mathbf{H}$ whose non-zero components are defined by $\mathbf{a}_x$. The term $\mathbf{a}_x$, which includes all significant off-diagonal elements relative to the Hessian diagonal, represents the offset of points within a point spread function (PSF) around each image point. By approximating the Hessian in equation 3.4 with equation 3.10, the cost savings is given by

$$\left(\frac{N_{\mathbf{x}_T} \times N_{\mathbf{a}_x}}{N_{\mathbf{x}} \times N_{\mathbf{x}}}\right) = \left(\frac{n_{x_T} n_{y_T} n_{z_T}}{n_x n_y n_z}\right) \times \left(\frac{n_{a_x} n_{a_y} n_{a_z}}{n_x n_y n_z}\right), \tag{3.11}$$

where, $N_{\mathbf{x}_T} = n_{x_T} n_{y_T} n_{z_T}$ is the number of samples in the target-area, $N_{\mathbf{a}_x} = n_{a_x} n_{a_y} n_{a_z}$ is the number of off-diagonal elements, and $N_{\mathbf{x}} = n_x n_y n_z$ is the number of elements in

the full model space. Valenciano (2008) discusses in detail the target-oriented Hessian and computational savings for different acquisition geometries.

Although the target-oriented Hessian (equation 3.10) is several orders of magnitudes cheaper than the full Hessian (equation 3.4), for a typical field seismic data set, explicit computation can be expensive and impractical. Tang (2011) show that by using phase-encoding methods, the target-oriented Hessian can be computed efficiently at orders of magnitude more cheaply than explicit implementation of equation 3.4. Where applicable, I randomly encode the receiver-side Green's functions, for which the target-oriented Hessian is given by

$$\widetilde{H}\left(\mathbf{x}_T, \mathbf{x}_{T+a_x}\right)) = \sum_{\mathbf{z}_r} \sum_{w} \omega^4 \sum_{\mathbf{x}_s} |f(s)|^2 G(\mathbf{x}_s, \mathbf{x}_T, \omega) \bar{G}(\mathbf{x}_s, \mathbf{x}_{T+a_x}, \omega) \times R(\mathbf{x}_T, \mathbf{x}_s, \mathbf{z}_r, \omega) \bar{R}(\mathbf{x}_{T+a_x}, \mathbf{x}_s, \mathbf{z}_r, \omega), \tag{3.12}$$

where $R(\mathbf{x}_T, \mathbf{x}_s, \mathbf{z}_r, \omega)$ denotes a random realization $\mathbf{z}_r$ of the receiver wavefield for shot $\mathbf{x}_s$. When summed over several random realizations, equation 3.12 is approximately equivalent to equation 3.10. Each random realization of the receiver wavefield is defined as (Tang, 2011)

$$R(\mathbf{x}_T, \mathbf{x}_s, \mathbf{z}_r, \omega) = \sum_{\mathbf{x}_r} W(\mathbf{x}_r, \mathbf{x}_s) G(\mathbf{x}_r, \mathbf{x}, \omega) \alpha(\mathbf{x}_r, \mathbf{z}_r, \omega), \tag{3.13}$$

where $W(\mathbf{x}_r, \mathbf{x}_s)$ is a geometry mask, and $\alpha(\mathbf{x}_r, \mathbf{z}_r, \omega)$ is a random phase-encoding function. Tang (2011) provides detailed derivation of equation 3.12 and discussions on the associated cost savings.

TIME-LAPSE SEISMIC IMAGING BY LEAST-SQUARES INVERSION

In time-lapse seismic imaging, several data sets acquired at different times over an evolving reservoir must be imaged such that only those image differences that reflect acoustic property changes due to production (or injection) are preserved.

Conventionally, a time-lapse image is computed as the difference between a baseline image $\tilde{\mathbf{m}}_0$ and a monitor image $\tilde{\mathbf{m}}_i$ obtained via migration:

$$\Delta\tilde{\mathbf{m}}_{0i} = \mathbf{L}_i^T\mathbf{d}_i - \mathbf{L}_0^T\mathbf{d}_0 = \tilde{\mathbf{m}}_i - \tilde{\mathbf{m}}_0, \tag{3.14}$$

where $\Delta\tilde{\mathbf{m}}_{0i}$ is the migrated time-lapse image between baseline (survey 0) and monitor (survey i). A time-lapse image computed this way has several undesirable artifacts that contaminate the time-lapse amplitudes of interest. As I discussed in chapter 2, in many cases, such artifacts can be attenuated by cross-equalization methods.

Instead of computing the time-lapse image as a difference between migrated images $\tilde{\mathbf{m}}_i$, we can compute it as a difference between inverted images $\hat{\mathbf{m}}_i$. In the data domain, the cost function defined for each individual experiment i can be minimized as follows:

$$S(\hat{\mathbf{m}}_i) = \|\mathbf{L}_i\mathbf{m}_i - \mathbf{d}_i^{obs}\|_2 \approx 0, \tag{3.15}$$

which in the image domain is equivalent to solving the system of equations given by

$$\mathbf{H}_i\hat{\mathbf{m}}_i \approx \tilde{\mathbf{m}}_i. \tag{3.16}$$

The inverted time-lapse image $\Delta\hat{\mathbf{m}}_{0i}$ is then given by

$$\Delta\hat{\mathbf{m}}_{0i} = \hat{\mathbf{m}}_i - \hat{\mathbf{m}}_0. \tag{3.17}$$

As noted earlier, computing the time-lapse image $\Delta\hat{\mathbf{m}}_{0i}$ from images obtained by solving equation 3.15 or equation 3.16 is called separate inversion. Separate inversion only allows us to introduce spatial constraints in the inversion.

For each survey, the spatially-regularized data domain inversion involves minimizing the cost function:

$$S(\hat{\mathbf{m}}_i) = \|\mathbf{L}_i\mathbf{m}_i - \mathbf{d}_i^{obs}\|_2 + \|\epsilon_i\mathbf{A}_i\mathbf{m}_i\|_2 \approx 0, \tag{3.18}$$

where $\mathbf{A}_i$ is a spatial regularization operator and ϵ_i is the spatial regularization parameter, which determines the relative weighting between image-fitting and spatial constraints. The equivalent regularized image-domain inversion requires a solution to the following system of equations:

$$\left[\mathbf{H}_i + \epsilon_i^2 \mathbf{A}_i^T \mathbf{A}_i\right] \hat{\mathbf{m}}_i \approx \tilde{\mathbf{m}}_i, \tag{3.19}$$

or simply

$$\left[\mathbf{H}_i + \mathring{\mathbf{A}}_i\right] \hat{\mathbf{m}}_i \approx \tilde{\mathbf{m}}_i, \tag{3.20}$$

where $\mathring{\mathbf{A}}_i = \epsilon_i^2 \mathbf{A}_i^T \mathbf{A}_i$. Because the operators defined on the right-hand-side of equation 3.20 may not be positive-definite, to solve the image-domain problem with a conjugate-gradients algorithm, we can solve a new least-squares fitting problem

$$\|\mathbf{H}_i \hat{\mathbf{m}}_i - \tilde{\mathbf{m}}_i\|_2 + \|\epsilon \mathbf{A}_i \hat{\mathbf{m}}_i\|_2 \approx 0. \tag{3.21}$$

Although solving equation 3.21 instead of equation 3.20 squares the condition number of the image-fitting problem, it ensures stable convergence.

As I show in chapter 4, although spatial regularization in linearized inversion improves the structural imaging of seismic data sets, it provides only limited improvements to time-lapse images. In the next section, I discuss the formulation of time-lapse seismic imaging as joint least-squares problems, which allow introduction of both spatial and temporal constraints into the inversion.

Joint least-squares inversion

For simplicity, in this section, I assume that there are two data sets (baseline $\mathbf{d}_0$ and monitor $\mathbf{d}_1$) acquired at different times. Below, I describe two methods of computing time-lapse images by joint inversion, namely: joint inversion for image differences, and joint inversion of multiple images.

Joint inversion for image differences (JID)

I formulate the joint modeling of the two data sets as follows:

$$\begin{bmatrix} \mathbf{L}_0 & \mathbf{0} \\ \mathbf{L}_1 & \mathbf{L}_1 \end{bmatrix} \begin{bmatrix} \mathbf{m}_0 \\ \mathbf{\Delta m} \end{bmatrix} = \begin{bmatrix} \mathbf{d}_0 \\ \mathbf{d}_1 \end{bmatrix}, \tag{3.22}$$

which can be divided into the following two parts:

$$\mathbf{L}_0\mathbf{m}_0 = \mathbf{d}_0, \tag{3.23}$$

$$\mathbf{L}_1\mathbf{m}_0 + \mathbf{L}_1\mathbf{\Delta m} = \mathbf{d}_1, \tag{3.24}$$

which are the modeling equations for the baseline survey (equation 3.23) and for the monitoring survey (equation 3.24). The time-lapse reflectivity image $\mathbf{\Delta m}$ is given by

$$\mathbf{\Delta m} = \mathbf{m}_1 - \mathbf{m}_0. \tag{3.25}$$

Kinematic corrections for geomechanical changes

An inherent assumption in equation 3.22 is that both $\mathbf{m}_0$ and $\mathbf{m}_1$ are collocated. This suggests that there are no physical movements of the reflector between the baseline and the monitor surveys. In addition, equation 3.22 assumes that there are no overburden velocity changes. In reality, stress changes associated with production (or injection) can cause physical movement of a subsurface point from baseline position $\mathbf{x}_0(x_0, y_0, z_0)$ in $\mathbf{m}_0$ to monitor position $\mathbf{x}_1(x_1, y_1, z_1)$ in $\mathbf{m}_1$.

First, let us assume that the correct migration velocities for the baseline and monitor data sets are available. If there is are stress-induced physical movements of subsurface points, equation 3.24 can be updated such that during modeling, a point at position $\mathbf{x}_0$ in $\mathbf{m}_0$ is repositioned/warped to position $\mathbf{x}_1$. An important assumption here—and in time-lapse imaging in general—is that residual errors introduced by this kinematic image correction are of smaller magnitudes than the reflectivity change of

interest. The updated monitor data modeling (equation 3.24) then becomes

$$\mathbf{L}_1\mathbf{S}^{m-}\mathbf{m}_0 + \mathbf{L}_1(\mathbf{m}_1 - \mathbf{S}^{m-}\mathbf{m}_0) = \mathbf{L}_1\mathbf{S}^{m-}\mathbf{m}_0 + \mathbf{L}_1\Delta\mathbf{m}^m = \mathbf{d}_1, \tag{3.26}$$

where $\mathbf{S}^{m-}$ is an orthogonal warping operator that aligns $\mathbf{m}_0$ to $\mathbf{m}_1$, and

$$\Delta\mathbf{m}^m = \mathbf{m}_1 - \mathbf{S}^{m-}\mathbf{m}_0 \tag{3.27}$$

is the time-lapse image estimated at the monitor position $\mathbf{x}_1$. Therefore, I re-write the baseline and monitor data modeling defined in equation 3.22 as follows:

$$\begin{bmatrix} \mathbf{L}_0 & \mathbf{0} \\ \mathbf{L}_1\mathbf{S}^{m-} & \mathbf{L}_1 \end{bmatrix} \begin{bmatrix} \mathbf{m}_0 \\ \Delta\mathbf{m}^m \end{bmatrix} \approx \begin{bmatrix} \mathbf{d}_0 \\ \mathbf{d}_1 \end{bmatrix}. \tag{3.28}$$

Note in equation 3.28 that to define the warping operator $\mathbf{S}^{m-}$, the true monitor reflector position must be known. This information can be obtained from a geomechanical model, or since I have so far assumed that the monitor data are imaged with the true monitor velocity, from misalignments between migrated baseline and monitor images. Where there are neither velocity change nor stress-induced compaction between surveys, $\mathbf{S}^{m-}$ becomes an identity operator. Furthermore, note that equation 3.28, requires that any regularization on the time-lapse image must be applied at the monitor position, or by first repositioning the time-lapse image to the baseline position as follows:

$$\Delta\mathbf{m} = \Delta\mathbf{m}^b = \mathbf{S}^{m+}\Delta\mathbf{m}^m, \tag{3.29}$$

where $\Delta\mathbf{m}^b$ is the time-lapse image at the baseline position, and $\mathbf{S}^{m+} \approx (\mathbf{S}^{m-})^{-1}$ is an operator that repositions events from the monitor position to the baseline position.

In the data domain, the inverted baseline image $\mathbf{m}_0$ and time-lapse image $\Delta\mathbf{m}$ can be obtained by minimizing the cost function r_d:

$$\left|\left|\begin{bmatrix} \mathbf{L}_0 & \mathbf{0} \\ \mathbf{L}_1\mathbf{S}^{m-} & \mathbf{L}_1 \end{bmatrix} \begin{bmatrix} \mathbf{m}_0 \\ \Delta\mathbf{m}^m \end{bmatrix} - \begin{bmatrix} \mathbf{d}_0 \\ \mathbf{d}_1 \end{bmatrix}\right|\right|^2 = r_d \approx 0. \tag{3.30}$$

In the image domain, $\hat{\mathbf{m}}_0$ and $\boldsymbol{\Delta}\hat{\mathbf{m}}^m$ can be obtained by solving the system

$$\begin{bmatrix} \mathbf{L}_0^T\mathbf{L}_0 + \mathbf{S}^{m+}\mathbf{L}_1^T\mathbf{L}_1\mathbf{S}^{m-} & \mathbf{S}^{m+}\mathbf{L}_1^T\mathbf{L}_1 \\ \mathbf{L}_1^T\mathbf{L}_1\mathbf{S}^{m-} & \mathbf{L}_1^T\mathbf{L}_1 \end{bmatrix} \begin{bmatrix} \hat{\mathbf{m}}_0 \\ \boldsymbol{\Delta}\hat{\mathbf{m}}^m \end{bmatrix} \approx \begin{bmatrix} \mathbf{L}_0^T & \mathbf{S}^{m+}\mathbf{L}_1^T \\ \mathbf{0} & \mathbf{L}_1^T \end{bmatrix} \begin{bmatrix} \mathbf{d}_0 \\ \mathbf{d}_1 \end{bmatrix}, \tag{3.31}$$

or simply

$$\begin{bmatrix} \mathbf{H}_0 + \mathbf{S}^{m+}\mathbf{H}_1\mathbf{S}^{m-} & \mathbf{S}^{m+}\mathbf{H}_1 \\ \mathbf{H}_1\mathbf{S}^{m-} & \mathbf{H}_1 \end{bmatrix} \begin{bmatrix} \hat{\mathbf{m}}_0 \\ \boldsymbol{\Delta}\hat{\mathbf{m}}^m \end{bmatrix} \approx \begin{bmatrix} \tilde{\mathbf{m}}_0 + \mathbf{S}^{m+}\tilde{\mathbf{m}}_1 \\ \tilde{\mathbf{m}}_1 \end{bmatrix}. \tag{3.32}$$

Again, note in equation 3.32 that the time-lapse image obtained is $\boldsymbol{\Delta}\hat{\mathbf{m}}^m$ at the monitor position and not $\boldsymbol{\Delta}\hat{\mathbf{m}} = \boldsymbol{\Delta}\hat{\mathbf{m}}^b$ at the baseline position. As shown later in this section, this formulation can be re-written in terms of $\boldsymbol{\Delta}\hat{\mathbf{m}}^b$.

Now, let us consider the case where the monitor data are imaged with the baseline velocity. In this scenario, equation 3.31 then becomes

$$\begin{bmatrix} \mathbf{L}_0^T\mathbf{L}_0 + \mathbf{S}^{\alpha+}\check{\mathbf{L}}_1^T\mathbf{L}_1\mathbf{S}^{m-} & \mathbf{S}^{\alpha+}\check{\mathbf{L}}_1^T\mathbf{L}_1 \\ \check{\mathbf{L}}_1^T\mathbf{L}_1\mathbf{S}^{m-} & \check{\mathbf{L}}_1^T\mathbf{L}_1 \end{bmatrix} \begin{bmatrix} \hat{\mathbf{m}}_0 \\ \boldsymbol{\Delta}\hat{\mathbf{m}}^m \end{bmatrix} \approx \begin{bmatrix} \mathbf{L}_0^T & \mathbf{S}^{\alpha+}\check{\mathbf{L}}_1^T \\ \mathbf{0} & \check{\mathbf{L}}_1^T \end{bmatrix} \begin{bmatrix} \mathbf{d}_0 \\ \mathbf{d}_1 \end{bmatrix}, \tag{3.33}$$

where $\check{\mathbf{L}}_1^T$, the migration operator with the monitor geometry but with baseline velocity, images the monitor data to apparent position $\mathbf{x}_1'(x_1', y_1', z_1')$. The operator $\mathbf{S}^{\alpha+}$ repositions the migrated image from $\mathbf{x}_1'$ to $\mathbf{x}_0$.

Because the operator $\mathbf{L}_1$ is a function of the true monitor velocity, if the true monitor velocity is known, we should solve equation 3.32 instead of equation 3.33. Where the monitor migration velocity is the correct one, equation 3.32 and equation 3.33 are equivalent. In most cases, the baseline velocity is a good approximation to the monitor velocity, resulting in only small kinematic errors in the monitor image. Where the change in velocity between surveys is large, kinematic corrections with a warping operator may be insufficient. In such scenario, it may be necessary to take into account such changes in computation of the monitor Hessian. One way to do this is by using the apparent displacements between the baseline and monitor images to update the Green's functions in the monitor Hessian. However, for the examples

considered in this thesis, I assume that kinematic errors introduced by imaging the monitor data with the baseline velocity are small enough that kinematic corrections with a warping operator are sufficient.

Inverting for the time-lapse image at the baseline position

If the monitor data are imaged with the correct velocity, to directly invert for $\mathbf{\Delta\hat{m}}^b = \mathbf{\Delta\hat{m}}$ at the baseline position, I make the substitution

$$\mathbf{\Delta m}^m = \mathbf{S}^{m-}\mathbf{\Delta m} \tag{3.34}$$

into equation 3.30 to obtain

$$\begin{bmatrix} \mathbf{L}_0 & \mathbf{0} \\ \mathbf{L}_1\mathbf{S}^{m-} & \mathbf{L}_1\mathbf{S}^{m-} \end{bmatrix} \begin{bmatrix} \mathbf{m}_0 \\ \mathbf{\Delta m} \end{bmatrix} \approx \begin{bmatrix} \mathbf{d}_0 \\ \mathbf{d}_1 \end{bmatrix} . \tag{3.35}$$

Therefore, in the data domain, $\mathbf{\hat{m}}_0$ and $\mathbf{\Delta\hat{m}}$ can be obtained by minimizing the objective function:

$$\left\| \begin{bmatrix} \mathbf{L}_0 & \mathbf{0} \\ \mathbf{L}_1\mathbf{S}^{m-} & \mathbf{L}_1\mathbf{S}^{m-} \end{bmatrix} \begin{bmatrix} \mathbf{\hat{m}}_0 \\ \mathbf{\hat{\Delta}m} \end{bmatrix} - \begin{bmatrix} \mathbf{d}_0 \\ \mathbf{d}_1 \end{bmatrix} \right\|^2 = r_d \approx 0 \ , \tag{3.36}$$

which leads to the image-domain formulation

$$\begin{bmatrix} \mathbf{H}_0 + \mathbf{S}^{m+}\mathbf{H}_1\mathbf{S}^{m-} & \mathbf{S}^{m+}\mathbf{H}_1\mathbf{S}^{m-} \\ \mathbf{S}^{m+}\mathbf{H}_1\mathbf{S}^{m-} & \mathbf{S}^{m+}\mathbf{H}_1\mathbf{S}^{m-} \end{bmatrix} \begin{bmatrix} \mathbf{\hat{m}}_0 \\ \mathbf{\Delta\hat{m}} \end{bmatrix} \approx \begin{bmatrix} \mathbf{\tilde{m}}_0 + \mathbf{S}^{m+}\mathbf{\tilde{m}}_1 \\ \mathbf{S}^{m+}\mathbf{\tilde{m}}_1 \end{bmatrix} = \begin{bmatrix} \mathbf{\tilde{m}}_0 + \mathbf{\tilde{m}}_1^b \\ \mathbf{\tilde{m}}_1^b \end{bmatrix} , \tag{3.37}$$

where $\mathbf{\tilde{m}}_1^b$, the migrated monitor image repositioned to the baseline position $\mathbf{x}_0$, is defined as

$$\mathbf{\tilde{m}}_1^b = \mathbf{S}^{m+}\mathbf{\tilde{m}}_1. \tag{3.38}$$

If the monitor data are imaged with the baseline velocity, provided velocity and stress-induced geomechanical changes are small, equation 3.37 can be approximated

as follows:

$$\begin{bmatrix} \mathbf{H}_0 + \mathbf{S}^{\alpha+}\check{\mathbf{H}}_1\mathbf{S}^{\alpha-} & \mathbf{S}^{\alpha+}\check{\mathbf{H}}_1\mathbf{S}^{\alpha-} \\ \mathbf{S}^{\alpha+}\check{\mathbf{H}}_1\mathbf{S}^{\alpha-} & \mathbf{S}^{\alpha+}\check{\mathbf{H}}_1\mathbf{S}^{\alpha-} \end{bmatrix} \begin{bmatrix} \hat{\mathbf{m}}_0 \\ \boldsymbol{\Delta}\hat{\mathbf{m}} \end{bmatrix} \approx \begin{bmatrix} \tilde{\mathbf{m}}_0 + \mathbf{S}^{\alpha+}\tilde{\mathbf{m}}_1^a \\ \mathbf{S}^{\alpha+}\tilde{\mathbf{m}}_1^a \end{bmatrix} = \begin{bmatrix} \tilde{\mathbf{m}}_0 + \tilde{\mathbf{m}}_1^b \\ \tilde{\mathbf{m}}_1^b \end{bmatrix}, \tag{3.39}$$

where,

$$\mathbf{S}^{\alpha+}\tilde{\mathbf{m}}_1^a \approx \tilde{\mathbf{m}}_1^b = \mathbf{S}^{m+}\tilde{\mathbf{m}}_1, \tag{3.40}$$

and $\tilde{\mathbf{m}}_1^a$ is the monitor image at position $\mathbf{x}'$ obtained by migrating the monitor data by the baseline velocity.

As previously stated, to arrive at equation 3.40, I assume that the amplitude errors that are caused by imaging the monitor data with the baseline velocity are negligible compared to the amplitude differences that are caused by production-induced changes in acoustic properties of the reservoir. Furthermore, as shown in Appendix A, provided our assumption of small kinematic errors holds, the migrated monitor image can be approximated as follows:

$$(\mathbf{L}_1^b)^T\mathbf{L}_1^b\mathbf{m}_1^b \approx \mathbf{S}^{m+}\mathbf{L}_1^T\mathbf{L}_1\mathbf{S}^{m-}\mathbf{m}_1^b \approx \mathbf{S}^{m+}\mathbf{L}_1^T\mathbf{d}_1 \approx \mathbf{S}^{\alpha+}\tilde{\mathbf{m}}_1^a \approx \tilde{\mathbf{m}}_1^b, \tag{3.41}$$

where, $(\mathbf{L}_1^b)^T\mathbf{L}_1^b = \mathbf{H}_1^b$ is the Hessian computed using the baseline velocity but with the monitor geometry. Substituting these into equation 3.37, I arrive at the the JID formulation:

$$\begin{bmatrix} \mathbf{H}_0 + \mathbf{H}_1^b & \mathbf{H}_1^b \\ \mathbf{H}_1^b & \mathbf{H}_1^b \end{bmatrix} \begin{bmatrix} \hat{\mathbf{m}}_0 \\ \boldsymbol{\Delta}\hat{\mathbf{m}} \end{bmatrix} \approx \begin{bmatrix} \tilde{\mathbf{m}}_0 + \tilde{\mathbf{m}}_1^b \\ \tilde{\mathbf{m}}_1^b \end{bmatrix}. \tag{3.42}$$

Because the formulation in equation 3.42 enables corrections for kinematic errors in the migrated images, it does not require application of a warping operator at every iteration. In addition, an important feature of this formulation is that it allows for direct regularization of the time-lapse image. However, it may be desirable to invert directly for the individual seismic images. In the next section, I show how this can be accomplished.

Joint inversion of multiple images (JMI)

Instead of formulating the baseline and monitor data modeling in terms of a static baseline image and a time-lapse image (equation 3.22), I formulate it here in terms of the individual reflectivity images:

$$\begin{bmatrix} \mathbf{L}_0 & \mathbf{0} \\ \mathbf{0} & \mathbf{L}_1 \end{bmatrix} \begin{bmatrix} \mathbf{m}_0 \\ \mathbf{m}_1 \end{bmatrix} = \begin{bmatrix} \mathbf{d}_0 \\ \mathbf{d}_1 \end{bmatrix} . \tag{3.43}$$

Using the same procedure as in the previous section, if the monitor data are imaged with the correct velocity, we can invert jointly for the individual images in data domain by minimizing the following objective function:

$$\left\| \begin{bmatrix} \mathbf{L}_0 & \mathbf{0} \\ \mathbf{0} & \mathbf{L}_1 \end{bmatrix} \begin{bmatrix} \mathbf{m}_0 \\ \mathbf{m}_1 \end{bmatrix} - \begin{bmatrix} \mathbf{d}_0 \\ \mathbf{d}_1 \end{bmatrix} \right\|^2 = r_d \approx 0, \tag{3.44}$$

and in the image domain by solving the system:

$$\begin{bmatrix} \mathbf{H}_0 & \mathbf{0} \\ \mathbf{0} & \mathbf{H}_1 \end{bmatrix} \begin{bmatrix} \hat{\mathbf{m}}_0 \\ \hat{\mathbf{m}}_1 \end{bmatrix} \approx \begin{bmatrix} \tilde{\mathbf{m}}_0 \\ \tilde{\mathbf{m}}_1 \end{bmatrix} . \tag{3.45}$$

As in the previous section, to invert for all images collocated at the baseline position, equations 3.44 and 3.45 become

$$\left\| \begin{bmatrix} \mathbf{L}_0 & \mathbf{0} \\ \mathbf{0} & \mathbf{L}_1\mathbf{S}^{m-} \end{bmatrix} \begin{bmatrix} \mathbf{m}_0 \\ \hat{\mathbf{m}}_1^b \end{bmatrix} - \begin{bmatrix} \mathbf{d}_0 \\ \mathbf{d}_1 \end{bmatrix} \right\|^2 = r_d \approx 0, \tag{3.46}$$

and

$$\begin{bmatrix} \mathbf{H}_0 & \mathbf{0} \\ \mathbf{0} & \mathbf{S}^{m+}\mathbf{H}_1\mathbf{S}^{m-} \end{bmatrix} \begin{bmatrix} \hat{\mathbf{m}}_0 \\ \hat{\mathbf{m}}_1^b \end{bmatrix} \approx \begin{bmatrix} \tilde{\mathbf{m}}_0 \\ \tilde{\mathbf{m}}_1^b \end{bmatrix} , \tag{3.47}$$

respectively. As previously stated, where there are no stress-induced compaction or velocity changes, $\mathbf{S}^{m+}$ is an identity matrix. These JMI formulations are equivalent to the JID formulations presented in equations 3.36 and 3.37, respectively.

If the monitor data are imaged with the baseline velocity, using the same assumptions and procedure as in the previous section, equation 3.47 becomes

$$\begin{bmatrix} \mathbf{H}_0 & \mathbf{0} \\ \mathbf{0} & \mathbf{H}_1^b \end{bmatrix} \begin{bmatrix} \hat{\mathbf{m}}_0 \\ \hat{\mathbf{m}}_1^b \end{bmatrix} \approx \begin{bmatrix} \tilde{\mathbf{m}}_0 \\ \tilde{\mathbf{m}}_1^b \end{bmatrix} . \tag{3.48}$$

Inverting multiple data sets

As shown in Appendix B, both the JID and JMI formulations are directly extendable to any number of data sets. In the data domain, the JID formulation for n surveys requires minimization of the cost function

$$S(\hat{\mathbf{m}}_0, \boldsymbol{\Delta}\hat{\mathbf{m}}_1.., \boldsymbol{\Delta}\hat{\mathbf{m}}_n) = \; ||\mathbf{L}_0\mathbf{m}_0 - \mathbf{d}_0||^2 + \sum_{i=1}^{n} \left|\left| \left(\mathbf{L}_j \mathbf{m}_0^m + \sum_{j=1}^{i} \mathbf{L}_j \boldsymbol{\Delta}\mathbf{m}_j^m \right) - \mathbf{d}_i \right|\right|^2 , \tag{3.49}$$

where, $\boldsymbol{\Delta}\mathbf{m}_j^m = \mathbf{m}_j^m - \mathbf{m}_{j-1}^m$ is the time-lapse image between survey j and survey $j-1$, and, $\mathbf{m}_j^m$ is defined at the monitor j position. The JMI formulation requires a minimization of the objective function

$$S(\hat{\mathbf{m}}_0, .., \hat{\mathbf{m}}_n) = \sum_{i=0}^{n} ||\mathbf{L}_i\mathbf{m}_i - \mathbf{d}_i||^2 . \tag{3.50}$$

In Appendix B, I develop the equivalent image domain formulations for equations 3.49 and 3.50.

REGULARIZED JOINT INVERSION

The JID and JMI formulations described in the previous section allows us to regularize the time-lapse imaging problem in different ways. Neglecting numerical errors, without regularization, results from both methods are similar. As previously stated, an important advantage of joint (versus separate) inversion is that it allows incorporation of both spatial and temporal regularization in the inversion.

For the generalized JID case (equation 3.49), assuming all data are imaged with the correct velocity, spatio-temporally regularized inversion involves minimization of the objective function

$$\begin{aligned} S(\hat{\mathbf{m}}_0, \boldsymbol{\Delta}\hat{\mathbf{m}}_1.., \boldsymbol{\Delta}\hat{\mathbf{m}}_n) = \quad & ||\mathbf{L}_0\mathbf{m}_0 - \mathbf{d}_0||^2 + \sum_{i=1}^{n} \left|\left| \left(\mathbf{L}_j\mathbf{m}_0^m + \sum_{j=1}^{i} \mathbf{L}_j\boldsymbol{\Delta}\mathbf{m}_j^m \right) - \mathbf{d}_i \right|\right|^2 \\ & + ||\epsilon_0\mathbf{A}_0\mathbf{m}_0||^2 + \sum_{j=1}^{n} \left|\left|\epsilon_j\mathbf{A}_j\boldsymbol{\Delta}\mathbf{m}_j^m\right|\right|^2 \\ & \sum_{j=1}^{n} \left|\left|-\zeta_{j-1}\boldsymbol{\Lambda}_{j-1}\boldsymbol{\Delta}\mathbf{m}_{j-1}^m + \zeta_j\boldsymbol{\Lambda}_j\boldsymbol{\Delta}\mathbf{m}_j^m\right|\right|^2, \end{aligned} \tag{3.51}$$

where $\boldsymbol{\Lambda}_j$ is the temporal coupling operator, and ζ_j is the temporal regularization parameter. The other terms are as previously defined.

For the generalized JMI case (equation 3.49), spatio-temporally regularized inversion involves minimization of the objective function

$$S(\mathbf{m}_0, .., \mathbf{m}_n) = \sum_{i=0}^{n} ||\mathbf{L}_i\mathbf{m}_i - \mathbf{d}_i||^2 + \sum_{i=0}^{n} ||\epsilon_i\mathbf{A}_i\mathbf{m}_i||^2 + \sum_{i=1}^{n} ||\zeta_i\boldsymbol{\Lambda}_i(\mathbf{m}_{i-1}, \mathbf{m}_i)||^2, \tag{3.52}$$

where the parameters ϵ_i and ζ_i determine the strengths of the spatial and temporal regularization operators, $\mathbf{A}$ and $\boldsymbol{\Lambda}$ respectively. Equation 3.52 is similar to the method applied by Ajo-Franklin et al. (2005) to a spatio-temporally regularized ray-tomography problem. Throughout the rest of this dissertation, I refer to solving equation 3.51 as regularized joint inversion for image differences (RJID), and solving equation 3.52 as regularized joint inversion of multiple images (RJMI).

Although both formulations provide reliable results, the RJMI formulation is preferable. Importantly, solving the joint inversion problem using the RJMI formulation is cheaper. For example, in the data domain, the JMI formulation requires fewer modeling and migration calls per iteration, and, in the image domain, it requires fewer matrix-vector multiplications. In the next section, I discuss different ways of incorporating spatial and temporal constraints in the the RJMI formulation.

Regularized joint inversion of multiple images (RJMI)

For simplicity, I consider two data sets. In the RJMI formulation, because models are completely decoupled, different spatial regularizations (second term in equation 3.52) can be defined for the two images as follows:

$$\left\| \begin{bmatrix} \epsilon_0 \mathbf{A}_0 & \mathbf{0} \\ \mathbf{0} & \epsilon_1 \mathbf{A}_1 \end{bmatrix} \begin{bmatrix} \hat{\mathbf{m}}_0 \\ \hat{\mathbf{m}}_1 \end{bmatrix} \right\|^2 \approx 0 \ . \tag{3.53}$$

and the temporal coupling (third term in equation 3.52) is given by

$$\left\| \begin{bmatrix} -\zeta_0 \mathbf{\Lambda_0} & \zeta_1 \mathbf{\Lambda}_1 \end{bmatrix} \begin{bmatrix} \hat{\mathbf{m}}_0 \\ \hat{\mathbf{m}}_1 \end{bmatrix} \right\|^2 \approx 0 \ . \tag{3.54}$$

Therefore, in the data domain, the full spatio-temporally regularized inversion requires a minimization of the norm:

$$\left\| \left[\begin{array}{cc} \mathbf{L}_0 & \mathbf{0} \\ \mathbf{0} & \mathbf{L}_1 \\ \hline \epsilon_0 \mathbf{A}_0 & \mathbf{0} \\ \mathbf{0} & \epsilon_1 \mathbf{A}_1 \\ \hline -\zeta_0 \mathbf{\Lambda}_0 & \zeta_1 \mathbf{\Lambda}_1 \end{array} \right] \begin{bmatrix} \hat{\mathbf{m}}_0 \\ \hat{\mathbf{m}}_1 \end{bmatrix} - \left[\begin{array}{c} \mathbf{d}_0 \\ \mathbf{d}_1 \\ \hline \mathbf{0} \\ \mathbf{0} \\ \hline \mathbf{0} \end{array} \right] \right\|^2 \approx 0 \ , \tag{3.55}$$

which is equivalent to solving the image domain problem

$$\left(\begin{bmatrix} \mathbf{H}_0 & \mathbf{0} \\ \mathbf{0} & \mathbf{H}_1 \end{bmatrix} + \begin{bmatrix} \mathbf{A}_{00} & \mathbf{0} \\ \mathbf{0} & \mathbf{A}_{11} \end{bmatrix} + \begin{bmatrix} \mathbf{\Lambda}_{00} & -\mathbf{\Lambda}_{01} \\ -\mathbf{\Lambda}_{10} & \mathbf{\Lambda}_{11} \end{bmatrix} \right) \begin{bmatrix} \hat{\mathbf{m}}_0 \\ \hat{\mathbf{m}}_1 \end{bmatrix} \approx \begin{bmatrix} \tilde{\mathbf{m}}_0 \\ \tilde{\mathbf{m}}_1 \end{bmatrix}, \tag{3.56}$$

where $\mathbf{A}_{ii} = \epsilon_i^2 \mathbf{A}_i^T \mathbf{A}_i$ and $\mathbf{\Lambda}_{ij} = \zeta_i \mathbf{\Lambda}_i^T \zeta_j \mathbf{\Lambda}_j$ are the spatial and temporal constraints, respectively.

In this dissertation, to construct the spatial regularization operator $\mathbf{A}_i$, I first estimate dips on the baseline image. For this, I use the plane-wave destruction method

of Fomel (2002). Using the estimated dips, I then compute stable non-stationary dip-filters based on factorized directional Laplacians (Fomel et al., 2003; Hale, 2007). Figure 3.1 shows the impulse responses of the three-dimensional dip-filters derived from cascaded two-dimensional filters (Clapp, 2000, 2005; Tang, 2011) and by full 3D factorization. To construct the factorized three-dimensional directional Laplacians, I follow the approach of Fomel (2000). Figure 3.2 shows the filters derived from two different dip combinations and different ranges.

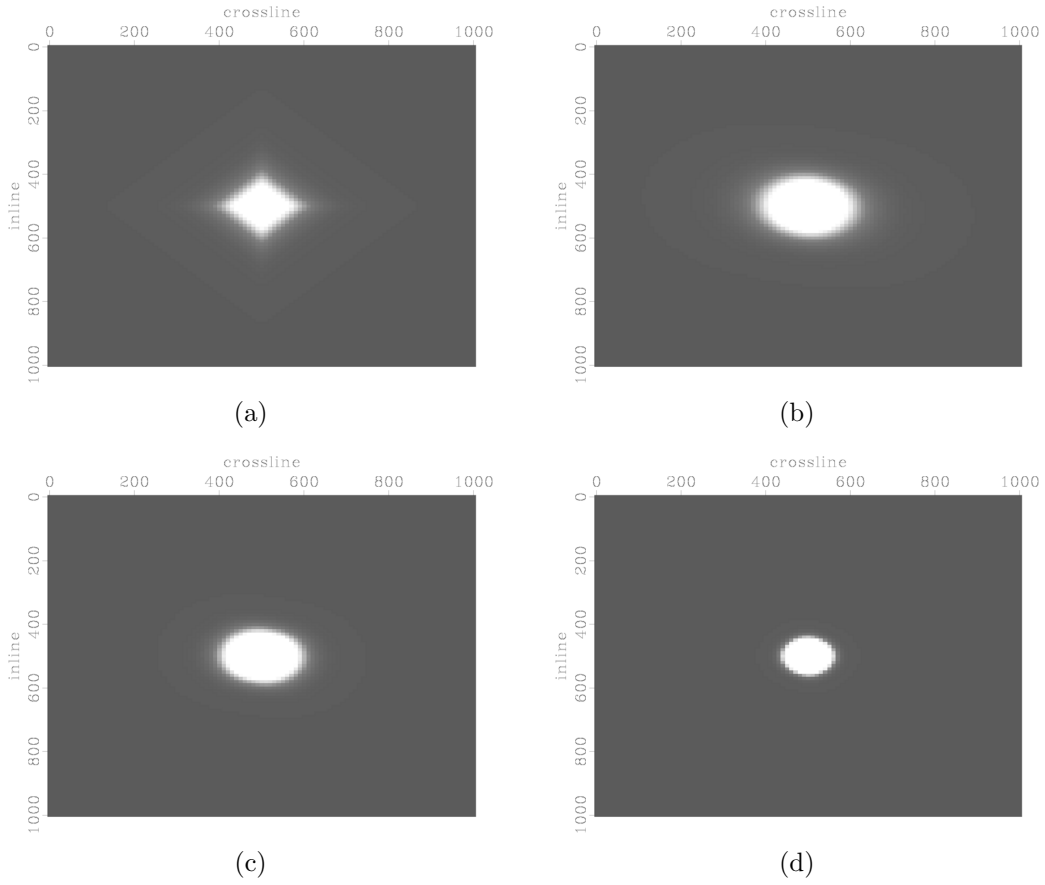

Figure 3.1: Two-dimensional slices through 3D impulse responses derived by cascaded two-dimensional filtering (a) and full 3D factorization (b)-(d). Note that the impulse responses derived from full factorization are more isotropic than the one derived from cascaded two-dimensional filtering. Furthermore, note that the filters in (b), (c), and (d) have large, medium and small ranges. [**ER**]. chap3/. imp-cascade,imp-0005,imp-005,imp-01

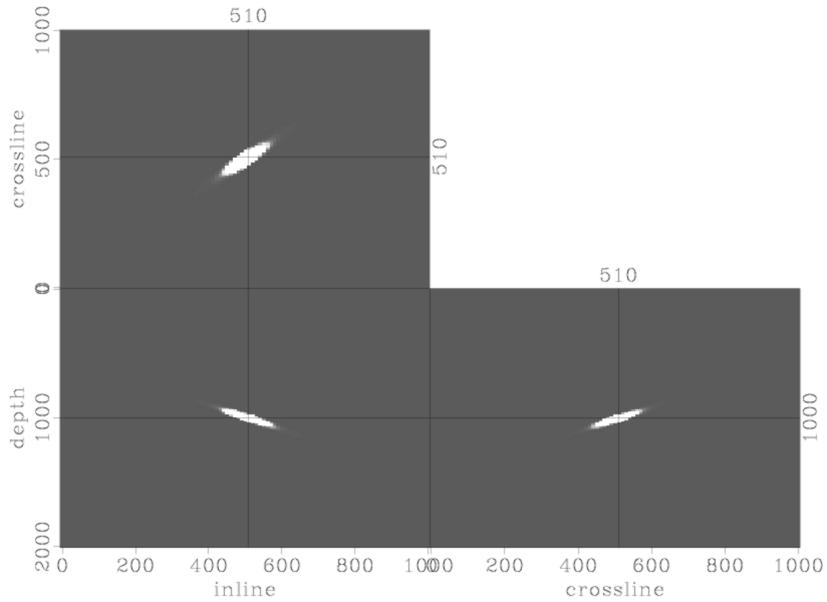

(a)

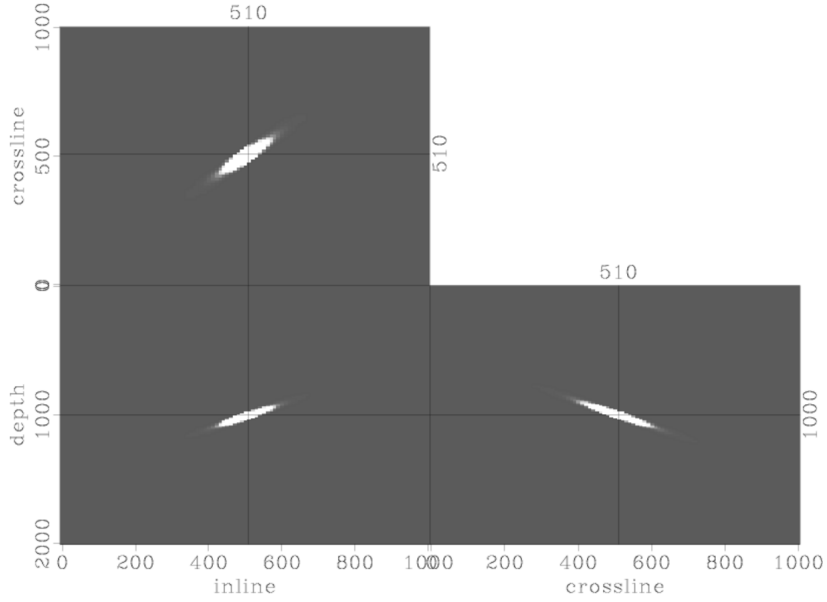

(b)

Figure 3.2: Impulse response for two different dip combinations derived from full factorization. The filter in (a) has a positive inline dip and negative crossline dip, whereas the filter in (b) has a negative inline dip and positive crossline dip. Furthermore, note that the filter in (a) has a smaller range than the filter in (b). [**ER**]. chap3/. imp-a,imp-b

In the RJMI formulation, these filters serve two important functions. First, they ensure smoothness along local dips that define the subsurface structure. In addition, by using variable filter ranges at different locations within and outside the reservoir, I limit the amount of temporal coupling and smoothness applied within and outside the reservoir region. This is important because it ensures that important time-lapse amplitude information within the reservoir is not destroyed by the regularization.

As I demonstrate in the next chapter, the choice of temporal regularization is also important. For example, if the images are collocated, it is straightforward to define a temporal constraint between the images. If the temporal regularization is a difference operator, equation 3.54 becomes

$$\left|\left|\zeta \begin{bmatrix} -\mathbf{I} & \mathbf{I} \end{bmatrix} \begin{bmatrix} \hat{\mathbf{m}}_0 \\ \hat{\mathbf{m}}_1 \end{bmatrix}\right|\right|^2 \approx 0 \ , \tag{3.57}$$

However, if the images are not collocated, in order to add any temporal regularization, the monitor image must first be warped to the baseline. For example, in the case where the temporal regularization is a difference operator, equation 3.54 becomes

$$\left|\left|\zeta \begin{bmatrix} -\mathbf{I} & \mathbf{S}^{m+} \end{bmatrix} \begin{bmatrix} \hat{\mathbf{m}}_0 \\ \hat{\mathbf{m}}_1 \end{bmatrix}\right|\right|^2 \approx 0 \ , \tag{3.58}$$

where, as previously defined, operator $\mathbf{S}^{m+}$ warps the monitor image to the baseline. Where the temporal operator includes some weighting (e.g. according to the illumination, or reservoir position), then equation 3.58 becomes

$$\left|\left|\zeta \mathbf{Q} \begin{bmatrix} -\mathbf{I} & \mathbf{S}^{m+} \end{bmatrix} \begin{bmatrix} \hat{\mathbf{m}}_0 \\ \hat{\mathbf{m}}_1 \end{bmatrix}\right|\right|^2 \approx 0 \ , \tag{3.59}$$

where $\mathbf{Q}$ defines the coupling characteristics according to predefined criteria. For example, regions with the poorest illumination may be assigned more larger weights than regions with high illumination. In addition, to preserve the time-lapse amplitude characteristics, regions outside the reservoir may be assigned a different coupling.

If the time-lapse image is to be computed at the baseline position, using the same procedure and assumptions as in the previous section, the regularized image-domain inversion problem is given by

$$\left(\begin{bmatrix} \mathbf{H}_0 & \mathbf{0} \\ \mathbf{0} & \mathbf{H}_1^b \end{bmatrix} + \begin{bmatrix} \mathbf{A}_{00} & \mathbf{0} \\ \mathbf{0} & \mathbf{A}_{11}^b \end{bmatrix} + \begin{bmatrix} \mathbf{\Lambda}_{00} & -\mathbf{\Lambda}_{01}^b \\ -\mathbf{\Lambda}_{10}^b & \mathbf{\Lambda}_{11}^b \end{bmatrix}\right) \begin{bmatrix} \hat{\mathbf{m}}_0 \\ \hat{\mathbf{m}}_1 \end{bmatrix} \approx \begin{bmatrix} \tilde{\mathbf{m}}_0 \\ \tilde{\mathbf{m}}_1 \end{bmatrix}, \quad (3.60)$$

where all operators and images are referenced to the baseline position. In Appendix B, I extend this formulation to an arbitrary number of surveys. In addition, I show how the formulation in equation 3.60 can be transformed into a preconditioned problem.

CONCLUSIONS

Time-lapse imaging can be posed as a joint linear least-squares problem. In this chapter, I have developed different formulations for regularized inversion of time-lapse seismic data sets in both the data domain and in the image domain. These inversion methods are suitable under different scenarios.

In chapter 4, using two- and three-dimensional synthetic data sets, I show how data-domain and image-domain inversion can be applied to different time-lapse imaging problems. In chapter 5, using two-dimensional field data sets, I show how time-lapse data sets can be conditioned to satisfy the assumptions made in this chapter. In addition, I show how time-lapse amplitudes in images derived from complete and incomplete data can be improved. In chapter 6, I show applications of image-domain inversion to complete and incomplete full-azimuth ocean-bottom-cable data sets.

As noted in this chapter, an important advantage of image-domain inversion is that, because it can be solved in a target-oriented manner, it is computationally inexpensive. Therefore it can be repeated quickly using different regularization parameters. I show in later chapters that by choosing different regularization parameters, regularized image-domain inversion can be used to obtain different plausible time-lapse images.

Because of its flexibility and easy parameterization, in all regularized image-domain examples, I use the RJMI formulation.

ACKNOWLEDGMENTS

In developing the methods in this chapter, I benefitted from previous work and collaborations with Alejandro Valenciano and Yaxun Tang.